

A brief overview of fixed-order perturbative QCD calculations of jet production in heavy-ion collisions

Ivan VITEV

Los Alamos National Laboratory

Theoretical Division, Group T-2, Mail Stop B283, Los Alamos, NM 87545, USA

We review recent developments in the QCD description of jet production and modification in reactions with heavy nuclei at relativistic energies. Our goal is to formulate a perturbative expansion in the presence of nuclear matter that allows to systematically improve the accuracy of the theoretical predictions. As an example, we present calculations of inclusive jet cross sections at RHIC, Z^0/γ^* -tagged jet cross sections at the LHC, and jet shapes that include both next-to-leading order perturbative effects and the effects of the nuclear medium.

§1. Introduction

In the past several years important developments in jet finding algorithms¹⁾ combined with advances in detector technology and experimental analysis have enabled, for the first time, measurements of jets²⁾ in nuclear reactions at very high energies at the Relativistic Heavy Ion Collider (RHIC).³⁾ Observation of jets is among the first physics results reported at the Large Hadron Collider (LHC),⁴⁾ which also has an active heavy-ion program.⁵⁾ In nucleus-nucleus (A+A) collisions, jet observables are expected to be much more discriminating⁶⁾ with respect to the underlying modes of parton propagation and energy loss in strongly-interacting matter⁷⁾ than existing studies of leading particles and leading particle correlations. Developments in theory are on the way to guide the heavy-ion experimental jet programs at RHIC and at the LHC and to help interpret current and upcoming physics results.

To take full advantage of jet physics, calculations at next-to-leading order (NLO) and beyond in perturbative Quantum Chromodynamics (QCD) are required.^{8),9)} In heavy-ion reactions there is the added complication of a soft background medium that these jets must traverse - the quark-gluon plasma (QGP). There are multiple ways to describe its properties that include but are not limited to temperature T , coupling strength $g^{\text{med.}}$, density ρ , energy density ϵ , parton rapidity density dN^g/dy , Debye screening scale m_D , parton mean free paths λ_q, λ_g , transport coefficient \hat{q} , and the strength of the background gluon field $\langle F^{+\perp} F_{\perp}^+ \rangle$. Relations between some of these quantities can be derived for specific models of the nuclear matter. In practice, however, one always needs independent constraints from experimental data or lattice simulations since the QGP that A+A reactions aim to produce may be strongly-coupled or non-perturbative.

The production of jets and the medium-induced bremsstrahlung at scales $Q^2 \sim E_T^2 \gg \Lambda_{QCD}^2$ and $Q^2 \sim (gT)E_T \gg \Lambda_{QCD}^2$, on the other hand, can be treated perturbatively. In fact, parton energy loss processes in the QGP and one-loop perturbative corrections are formally manifested in experimental observables at the same order

Medium \rightarrow	LO	NLO	NNLO	NNNLO	
Vacuum \downarrow					
LO	α_s^2	$\alpha_s^2(\alpha_s^{\text{med.}})$	$\alpha_s^2(\alpha_s^{\text{med.}})^2$	$\alpha_s^2(\alpha_s^{\text{med.}})^3$	\dots
NLO	α_s^3	$\alpha_s^3(\alpha_s^{\text{med.}})$	$\alpha_s^3(\alpha_s^{\text{med.}})^2$	$\alpha_s^3(\alpha_s^{\text{med.}})^3$	\dots
NNLO	α_s^4	$\alpha_s^4(\alpha_s^{\text{med.}})$	$\alpha_s^4(\alpha_s^{\text{med.}})^2$	$\alpha_s^4(\alpha_s^{\text{med.}})^3$	\dots

Table I. Perturbative expansion relevant to large Q^2 processes in the presence of a nuclear medium.

$\mathcal{O}(\alpha_s^3)$, $\mathcal{O}(\alpha_s^2\alpha_s^{\text{med.}})$. It should be noted, however, that the values of α_s and $\alpha_s^{\text{med.}}$ can differ considerably. The emerging perturbative expansion for jet production and modification in heavy-ion reactions can easily be generalized to higher orders and is shown in Table I. Self-consistent fixed-order theoretical calculations are the ones that take into consideration all terms along the counter diagonals of this matrix. At present, only inclusive $\alpha_s^{\text{med.}}$ induced gluon bremsstrahlung has been evaluated and the corresponding next-to-leading order jet calculations are presented below.

§2. Inclusive jet production at RHIC

At NLO, the inclusive and tagged jets cross sections can be expressed schematically as follows:

$$d\sigma_{jet(+\text{tag})} = \frac{1}{2!}d\sigma[2 \rightarrow 2]S_2(\{p, y, \phi\}_2) + \frac{1}{3!}d\sigma[2 \rightarrow 3]S_3(\{p, y, \phi\}_3). \quad (2.1)$$

Here, p_i, y_i, ϕ_i are the transverse momentum, rapidity, and azimuthal angle of the i -th particle ($i = 1, 2, 3$), respectively, and $\sigma[2 \rightarrow 2]$, $\sigma[2 \rightarrow 3]$ represent the production cross sections with two and three final-state partons. S_2 and S_3 are phase space constraints and $S_2 = \sum_{i=1}^2 S(i) = \sum_{i=1}^2 \delta(E_{T_i} - E_T)\delta(y_i - y)$ identifies the jet with its parent parton. Hence, it is only at next-to-leading order that the dependence of the experimental observables on the jet cone radius R , the jet finding algorithm, or the trigger particle energy can be theoretically investigated. For an angular separation $R_{ij} = \sqrt{(y_i - y_j)^2 + (\phi_i - \phi_j)^2}$, defined for any possible parton pair (i, j) ,

$$S_3 = \sum_{i < j} \delta(E_{T_i} + E_{T_j} - E_T) \delta\left(\frac{E_{T_i}y_i + E_{T_j}y_j}{E_{T_i} + E_{T_j}} - y\right) \theta(R_{ij} < R_{\text{rc}}) \quad (2.2)$$

$$+ \sum_i S(i) \prod_{j \neq i} \theta\left(R_{ij} > \frac{(E_{T_i} + E_{T_j})R}{\max(E_{T_i}, E_{T_j})}\right), R_{\text{rc}} = \min\left(R_{\text{sep}}R, \frac{E_{T_i} + E_{T_j}}{\max(E_{T_i}, E_{T_j})}R\right).$$

In Eq. (2.2) R_{rc} determines when two partons should be recombined in a jet. Here, $1 \leq R_{\text{sep}} \leq 2$ is introduced to take into account features of experimental cone algorithms, employed to improve infrared safety. Eq. (2.2) establishes a correspondence between the commonly used jet finders and the perturbative calculations to $\mathcal{O}(\alpha_s^3)$ with the goal of providing accurate predictions for comparison to data. For example, $R_{\text{sep}} = 2$ yields a midpoint cone algorithm and $R_{\text{sep}} = 1$ corresponds to the k_T algorithm.^{8),10)} R is the cone size or parton separation parameter, respectively. We have compared NLO calculation⁸⁾ of the inclusive jet cross section at $\sqrt{s} = 200$ GeV p+p

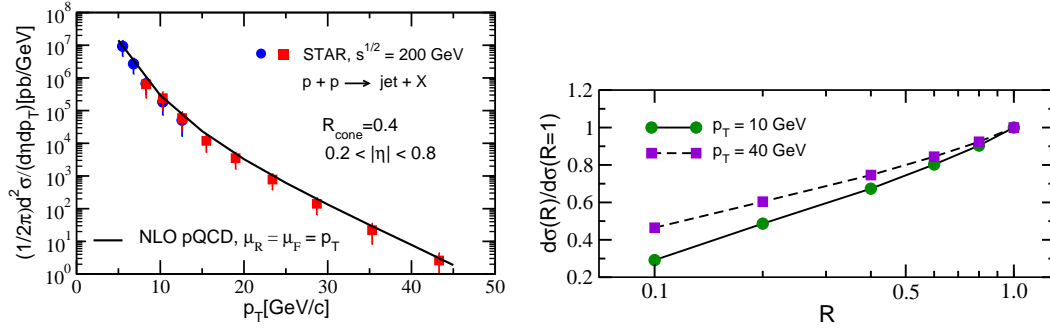


Fig. 1. Comparison of the NLO calculation to STAR experimental data¹¹⁾ on the inclusive jet cross section for $R=0.4$ (left panel). The variation of the jet cross section with the cone size R for $E_T = 10, 40$ GeV around midrapidity at RHIC is also shown (right panel).

collisions at RHIC to the STAR experimental measurement which uses a midpoint cone algorithm¹¹⁾ in the pseudorapidity range $0.2 \leq \eta \leq 0.8$. Very good agreement between data and theory is achieved with a standard choice for the renormalization and factorization scales $\mu_R = \mu_f = E_T$,¹²⁾ as shown in the left panel of Figure 1. Variation of these scales within $(E_T/2, 2E_T)$ leads to less than $(+10\%, -20\%)$ variation of the jet cross section. We also found that there is a significant dependence of $d\sigma^{\text{jet}}/dydE_T$ on the cone size R , which, even in p+p reactions, can exceed a factor of two. This is illustrated in the right panel of Figure 1. Analytically, the $\ln(R/R_0)$ scaling of the cross section can be understood from the $1/r$ angular behavior of the perturbative QCD splitting kernel at high energies.

When compared to a parton shower in the vacuum, the medium-induced quark and gluon splittings have noticeably different angular and lightcone momentum fraction dependencies.^{6), 13)} In particular, for energetic partons propagating in hot and dense QCD matter, the origin of the coherent suppression of their radiative energy loss, known as the Landau-Pomeranchuk-Migdal effect, can be traced to the cancellation of the collinear radiation at $r < m_D/\langle\omega(m_D, \lambda_g, E_T)\rangle$.¹³⁾ Here, the Debye screening scale $m_D \simeq gT$ and $\langle\omega\rangle \simeq$ few GeV. Thus, the medium-induced component of the jet, which is given by the properly normalized gluon bremsstrahlung intensity spectrum $\psi^{\text{med}}(r, R) \propto dI^{\text{rad}}/d\omega dr$ within the cone, has a characteristic large-angle distribution away from the jet axis. This is illustrated in Figure 2 for central Au+Au and central Cu+Cu collisions at RHIC. We emphasize that accurate numerical simulations, taking into account the geometry of the heavy-ion reaction, the longitudinal Bjorken expansion of the QGP, and the constraints imposed by its experimentally measured entropy density per unit rapidity,⁶⁾ have been performed for all physics results quoted here.

One can exploit the differences between the vacuum and the in-medium parton showers by varying the cone radius R ($R_{i,\text{jet}} < R$) and a cut p_T^{min} ($E_{T_i} > p_T^{\text{min}}$) for the particles " i " that constitute the jet, to gain sensitivity to the properties of the QGP and of the mechanisms of parton energy loss in hot and dense QCD matter.⁶⁾ This is illustrated in the insert of Figure 2. The most easily accessible experimental feature of jet production in nuclear collisions is, arguably, the suppression of the

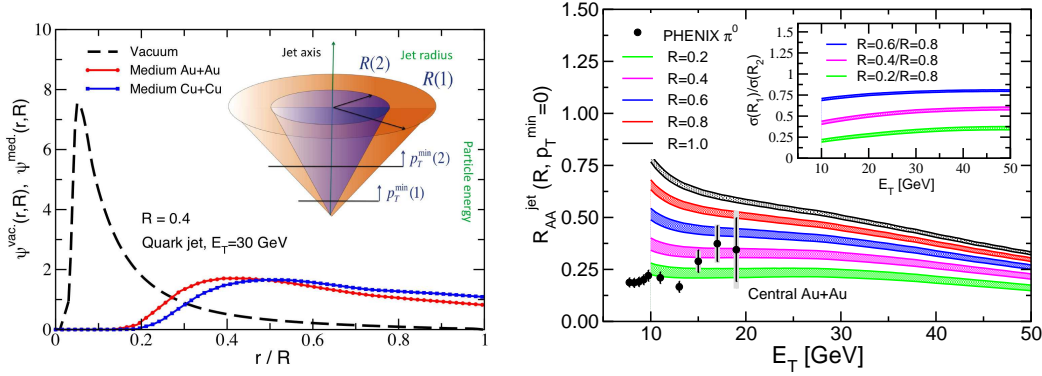


Fig. 2. The differential jet shape in vacuum $\psi^{\text{vac}}(r, R)$ is contrasted to the medium-induced contribution $\psi^{\text{med}}(r, R)$ by a $E_T = 30$ GeV quark in Au+Au and Cu+Cu collisions at $\sqrt{s_{NN}} = 200$ GeV. The insert illustrates a method for studying the characteristics of these parton showers (left panel). Transverse energy dependent nuclear modification factor R_{AA}^{jet} for different cone radii R in $b = 3$ fm Au+Au collisions. Inserts show ratios of jet cross sections for different R in nuclear reactions versus E_T (right panel).

inclusive cross section in heavy-ion reaction compared to the binary collision scaled, $\propto \langle N_{\text{bin}} \rangle$, production rate in elementary nucleon-nucleon reactions:¹²⁾

$$R_{AA}^{\text{jet}}(E_T; R, p_T^{\text{min}}) = \frac{d\sigma^{AA}(E_T; R, p_T^{\text{min}})}{dy d^2 E_T} \bigg/ \langle N_{\text{bin}} \rangle \frac{d\sigma^{pp}(E_T; R, p_T^{\text{min}})}{dy d^2 E_T}. \quad (2.3)$$

Eq. (2.3) defines a two dimensional jet attenuation pattern versus R and p_T^{min} for every fixed E_T . In contrast, for the same E_T , inclusive particle quenching is represented by a single value related to the $R \rightarrow 0$ and $p_T^{\text{min}} \gg \langle \omega \rangle$ limit in Eq. (2.3). Thus, jet observables are much more differential and, hence, immensely more powerful than leading particles and leading particle correlations in their ability to discriminate between the competing physics mechanisms of quark and gluon energy loss in dense QCD matter and between theoretical model approximations to parton dynamics in the QGP.

We calculate the medium-modified jet cross section per binary nucleon-nucleon scattering as follows ($p_T^{\text{min}} = 0$):

$$\frac{1}{\langle N_{\text{bin}} \rangle} \frac{d\sigma^{AA}(R)}{dy d^2 E_T} = \int_{\epsilon=0}^1 d\epsilon \sum_{q,g} P_{q,g}(\epsilon, E) \frac{1}{(1 - (1 - f_{q,g}) \cdot \epsilon)^2} \frac{d\sigma_{q,g}^{\text{CNM,NLO}}(R)}{dy d^2 E'_T}. \quad (2.4)$$

Here, $P_{q,g}(\epsilon, E)$ is the probability distribution for the parent quarks and gluons to lose a fraction $\epsilon = \sum_i \omega_i / E$ of their energy due to multiple gluon emission in the QGP. In Eq. (2.4) $d\sigma_{q,g}^{\text{CNM,NLO}}(R)/dy d^2 E'_T$ is the differential cross section which includes the known cold nuclear matter effects¹⁴⁾ and $(1 - f_{q,g}) \cdot \epsilon$ represents the fraction of the energy of the parent parton that the medium re-distributes outside of the cone of radius R . The measured cross section is then a probabilistic superposition of the cross sections of protojets of initially larger energy $E'_T = E_T / (1 - (1 - f_{q,g}) \cdot \epsilon)$. Our results for

the nuclear modification factor of inclusive jets R_{AA}^{jet} in central Au+Au collisions with $\sqrt{s_{NN}} = 200$ GeV at RHIC are presented in the right panel of Figure 2. Experimental data on leading π^0 suppression for these reactions is only included for reference. A continuous variation of R_{AA}^{jet} with the cone radius R is clearly observed and shows the sensitivity of the inclusive jet cross section in high-energy nuclear collisions to the characteristics of QGP-induced parton shower. For $R \leq 0.2$ the quenching of jets approximates the already observed suppression in the production rate of inclusive high- p_T particles. It should be noted that in our theoretical calculation CNM effects contribute close to 1/2 of the observed attenuation for $E_T \geq 30$ GeV. These can be dramatically reduced at all E_T by taking the ratio of two differential cross section measurements for different cone radii R_1 and R_2 , as shown in the insert.

§3. Z^0/γ^* -tagged jets at the LHC

We begin by discussing the cross section for Z^0/γ^* -tagged jet production in p+p collisions. It is instructive to first consider the leading order (LO) result, from which one can understand the underlying production processes and appreciate why the Z^0 boson was originally considered as a suitable tag for the initial associated jet energy.¹⁵⁾ In the collinear factorization approach, the Z^0/γ^* +jet cross section reads:

$$\frac{d\sigma}{dy_{(Z)} dy_{(\text{jet})} d^2\mathbf{p}_{T(Z)} d^2\mathbf{p}_{T(\text{jet})}} = \sum_{g,q,q} \frac{f(x_1, \mu) f(x_2, \mu) |M|^2}{(2\pi)^2 4 x_1 x_2 S^2} \delta^2(\mathbf{p}_{T(Z)} - \mathbf{p}_{T(\text{jet})}) . \quad (3.1)$$

Here, $f(x_i, \mu)$ are the parton distribution functions and $|M|^2$ are the relevant squared matrix elements. The δ -function constraint on the transverse momentum of the jet is valid only at this order and only at the partonic level.

The main advantage of the next-to-leading order Z^0/γ^* +jet+X calculation⁹⁾ is the ability to precisely predict the transverse momentum distribution of jets associated with a dimuon tag in a narrow p_T interval.¹⁶⁾ Beyond tree level, the momentum constraint that the Z^0 boson measurement provides is compromised by parton splitting and Z-strahlung processes. We demonstrate this in the left panel of Figure 3, which shows the differential cross section for jets tagged with $Z^0/\gamma^* \rightarrow \mu^+\mu^-$ in p+p collisions at $\sqrt{s_{NN}} = 4$ TeV. We implement acceptance cuts of $|y| < 2.5$ for both jets and final-state muons, and, as mentioned above, constrain the invariant mass of the dimuon pair to the interval $M_z \pm 3\Gamma_z$, where $M_z = 91.1876$ GeV and $\Gamma_z = 2.4952$ GeV. This is the kinematic acceptance range in which we will evaluate all results that follow and which can be easily adjusted to match upcoming experimental measurements. For the cross section shown in Figure 3, the tagging Z^0/γ^* is required to have $92.5 \text{ GeV} < p_T < 112.5 \text{ GeV}$. The LO result restricts the p_T of the jet to lie exactly within this interval, consistent with Eq. (3.1). As seen in the left panel of Figure 3, at NLO the deviations from this naive relation are very significant. We have included results for three different values of the jet cone radius, $R = 0.2, 0.4, 0.8$. The variation of the cross section with R around $p_{T(\text{jet})} \sim p_{T(Z)}$ arises from the interplay between the amount of energy that is contained in the jet and the number of reconstructed jets (one or two). For $p_{T(\text{jet})} \gg p_{T(Z)}$ or $p_{T(\text{jet})} \ll p_{T(Z)}$ the two

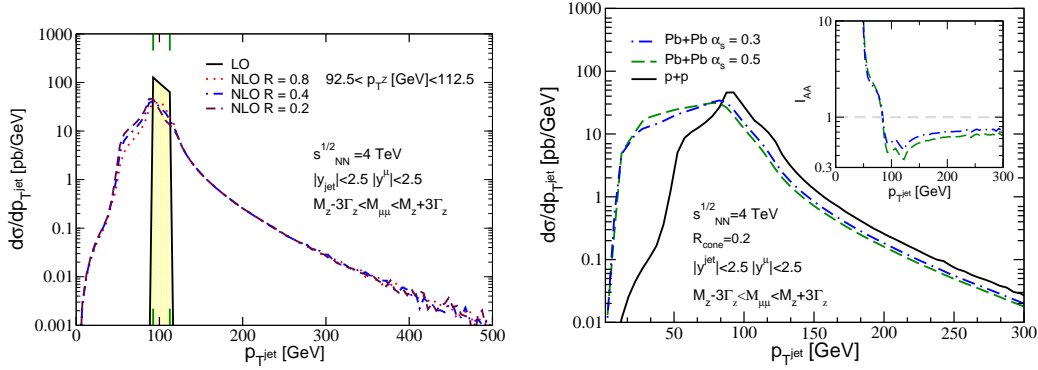


Fig. 3. Transverse momentum distributions of a jet associated with $Z^0/\gamma^*(\rightarrow \mu^+ + \mu^-)$ tag to $\mathcal{O}(G_F\alpha_s)$ and $\mathcal{O}(G_F\alpha_s^2)$ for transverse momentum cut $92.5 \text{ GeV} < p_T < 112.5 \text{ GeV}$ on the tagging particle (left panel). The NLO p_T -differential cross section per nucleon pair for these tagged jets in central Pb+Pb collisions at the LHC is also presented for a cone radius $R = 0.2$ (right panel). The ratio of the two cross sections is shown in the insert.

final-state partons are well-separated and identified as different jets. The falloff of the differential cross section relative to its peak value at $p_{T(\text{jet})} = p_T(Z)$ is then controlled by the QCD splitting kernel (the part related to the large lightcone parton momentum) and there is no dependence on the cone radius.

In order to quantify the inability of the Z^0/γ^* tag to constrain the momentum of the jet we calculate the mean $p_T \equiv \langle p_{T(\text{jet})} \rangle$ and standard deviation $\Delta p_{T(\text{jet})} = \sqrt{\langle p_{T(\text{jet})}^2 \rangle - \langle p_{T(\text{jet})} \rangle^2}$ for each of the curves in Figure 3. Our results are presented in Table 2. The standard deviation for the LO curves is not strictly zero because of the finite p_T width of the tagging Z^0/γ^* interval. The NLO curves exhibit a similar $\langle p_{T(\text{jet})} \rangle$ as the LO result, with $\langle p_{T(\text{jet})} \rangle$ increasing as the cone radius increases. However, in going from LO to NLO there is a significant jump in $\Delta p_{T(\text{jet})}$. The width of the jet momentum distribution quadruples for an energetic tag. The very large values of $\Delta p_{T(\text{jet})}/\langle p_{T(\text{jet})} \rangle \sim 25\%$ at NLO create serious complications for experimentally tagging the initial associated jet energy in both p+p and A+A collisions. While additional cuts can be considered, such as the requirement for a single jet within the experimental acceptance that is exactly opposite the tagging particle in azimuth, these will reduce the already small projected multiplicity for this final state in heavy-ion reactions.

Accounting for the fact that the Z^0/γ^* and their decay dileptons escape the region of dense nuclear matter unaffected by the strong interaction, the modified jet

$p_{T(Z)}$ [GeV]		LO	R = 0.2	R = 0.4	R = 0.8
92.5-112.5	$\langle p_{T(\text{jet})} \rangle$ [GeV]	100.79	93.91	96.63	100.05
	$\Delta p_{T(\text{jet})}$ [GeV]	6.95	25.19	24.88	24.15

Table II. Mean p_T and $\Delta\langle p_T \rangle$ for Z^0/γ^* -tagged jets at the LHC from LO and NLO calculation.

cross section can be calculated as follows:

$$\frac{d\sigma}{d^2\mathbf{p}_{(Z)}d^2\mathbf{p}_Q} = \sum_{q,g} \int d\epsilon \frac{P_{q,g}(\epsilon)}{[1 - (1 - f_{q,g})\epsilon]^2} \frac{d\sigma^{q,g}}{d^2\mathbf{p}_{(Z)}d^2\mathbf{p}_{(\text{jet})}} \left(\frac{\mathbf{p}_Q}{[1 - (1 - f_{q,g})\epsilon]} \right) . \quad (3.2)$$

Eq. (3.2) resembles the result for inclusive jet suppression and we have integrated over y_{jet} and y_Z in finite rapidity intervals. Our results are presented in the right panel of Figure 3, where the tagging Z^0/γ^* is required to have $92.5 \text{ GeV} < p_T < 112.5 \text{ GeV}$. The main physics effect that this figure illustrates is the QGP-induced modification to the vacuum parton shower. Specifically, its broadening¹³⁾ implies that part of the jet energy is redistributed outside of the jet cone and the differential jet distribution is downshifted toward smaller transverse momenta. The smaller the jet cone radius the more pronounced this effect is. As the jet cone radius is increased, the medium-modified curves approach the p+p result, as more and more of the medium-induced bremsstrahlung is recovered in the jet.

A generalization of the cross section ratios per binary nucleon-nucleon collisions for tagged jets,¹⁶⁾ I_{AA}^{jet} , is given in the insert in Figure 3. The variation in the magnitude of I_{AA}^{jet} at transverse momenta larger than the p_T of the tag is controlled by the shape of the jet spectrum. The most striking feature is the sharp transition from tagged jet suppression above $p_{T(Z)}$ to tagged jet enhancement below $p_{T(Z)}$. For the example shown in the left panel of Figure 3, the enhancement can be as large as a factor of ten. This transition from suppression to enhancement is a unique prediction of jet quenching for tagged jets and will constitute an unambiguous experimental evidence for strong final-state interactions and parton energy loss in the QGP.

§4. Jet shapes at RHIC and at the LHC

Integral and differential jet shapes, defined as:

$$\Psi_{\text{int}}(r, R) = \frac{\sum_i (E_T)_i \Theta(r - (R_{\text{jet}})_i)}{\sum_i (E_T)_i \Theta(R - (R_{\text{jet}})_i)} , \quad \psi(r, R) = \frac{d\Psi_{\text{int}}(r, R)}{dr} , \quad (4.1)$$

were historically the first observables used to study jet sub-structure and intra-jet energy flow.¹⁰⁾ To $\mathcal{O}(\alpha_s^3)$ $\psi(r, R)$ can be evaluated from the LO parton splitting functions in perturbative QCD¹⁰⁾ and the analytic results can be generalized to allow for a minimum particle or calorimeter tower energy p_T^{min} in the definition of the jet.⁶⁾ Such experimental cuts can be particularly useful in reducing the large background of soft particles in the high multiplicity environment of heavy-ion collisions.

Analytically, jet shapes are evaluated as follows:^{10), 6)}

$$\begin{aligned} \psi^{\text{vac.}}(r, R) = & \psi_{\text{coll}}(r, R) (P_{\text{Sudakov}}(r, R) - 1) + \psi_{\text{LO}}(r, R) \\ & + \psi_{i,\text{LO}}(r, R) + \psi_{\text{PC}}(r, R) + \psi_{i,\text{PC}}(r, R) . \end{aligned} \quad (4.2)$$

In Eq. (4.2) the first term represents the contribution from the Sudakov-resummed small-angle parton splitting; the second and third terms give the leading-order final-state and initial-state contributions, respectively; the last two terms come from power

corrections $\propto Q_0/E_T$, $Q_0 \simeq 2-3$ GeV, when one integrates over the Landau pole in the modified leading logarithmic approximation (MLLA). This approach was shown to provide a very good description of the differential intra-jet energy flow at the Tevatron,⁶⁾ as measured by CDF II.¹⁷⁾ Thus, reliable predictions for the jet substructure in p+p reactions at RHIC and the LHC can be obtained and used as a baseline to study the distortion of jet shapes in more complex systems, such as p+A and A+A.

Inclusive jet cross sections and jet shapes in nuclear collisions are closely related:^{6), 12)}

$$\psi_{\text{tot.}}\left(\frac{r}{R}\right) = \frac{\langle N_{\text{bin}} \rangle}{d\sigma^{AA}(R)/dyd^2E_T} \int_{\epsilon=0}^1 d\epsilon \sum_{q,g} \frac{P_{q,g}(\epsilon, E)}{(1 - (1 - f_{q,g}) \cdot \epsilon)^3} \quad (4.3)$$

$$\times \frac{d\sigma_{q,g}^{\text{CNM,NLO}}(R, E'_T)}{dyd^2E'_T} \left[(1 - \epsilon) \psi_{\text{vac.}}^{q,g}\left(\frac{r}{R}; E'\right) + f_{q,g} \cdot \epsilon \psi_{\text{med.}}^{q,g}\left(\frac{r}{R}; E'\right) \right].$$

It should be noted that vacuum and medium-induced parton showers become more collimated with increasing E'_T and the mean relative jet width,

$$\left\langle \frac{r}{R} \right\rangle = \int_0^1 d\left(\frac{r}{R}\right) \frac{r}{R} \psi\left(\frac{r}{R}\right), \quad (4.4)$$

is reduced.^{6), 12)} Consequently, the striking suppression pattern for jets, see for example the right panel of Figure 2, can be accompanied by a very modest growth in the observed $\langle r/R \rangle$. We show in Table III the relative widths in the vacuum, for a hypothetical case of complete parton energy loss ($P_{q,g}(\epsilon) = \delta(1 - \epsilon)$) that falls inside of R ($f_{q,g} = 1$), and for our realistic simulation of $E_T = 20, 50, 100$, and 200 GeV jets of $R = 0.4$ in central Pb+Pb collisions at the LHC. These numerical results show that there is very little $< 10\%$ increase in the magnitude of this observable. For Au+Au and Cu+Cu collisions at RHIC, we found that, on average, jet broadening is even smaller, $< 5\%$. Therefore, a rough 1-parameter characterization of energy flow in jets will not resolve the effect of the QGP medium.

Lastly, we point out where the anticipated jet broadening effects will be observed in the differential shape by studying the ratio $\psi_{\text{tot.}}(r/R)/\psi_{\text{vac.}}(r/R)$ in Figure 4. The left panel shows a simulation of the differential shape of a 100 GeV jet at the LHC. The right panel presents the ratio discussed above. We recall that the small

$R = 0.4$	Vacuum	Complete E-loss	Realistic case
$\langle r/R \rangle, E_T = 20\text{GeV}$	0.41	0.55	0.45
$\langle r/R \rangle, E_T = 50\text{GeV}$	0.35	0.48	0.38
$\langle r/R \rangle, E_T = 100\text{GeV}$	0.28	0.44	0.32
$\langle r/R \rangle, E_T = 200\text{GeV}$	0.25	0.40	0.28

Table III. Summary of mean relative jet radii $\langle r/R \rangle$ in the vacuum, with complete energy loss, and in the QGP medium. Shown are results for cone radii $R = 0.4$ and transverse energies $E_T = 20, 50, 100, 200$ GeV at $\sqrt{s} = 5.5$ TeV central Pb+Pb collisions at the LHC.

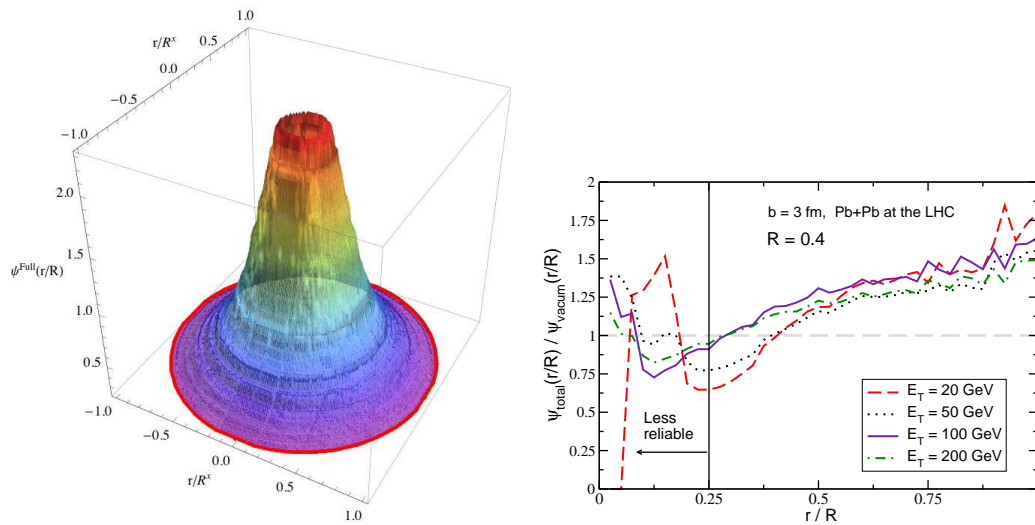


Fig. 4. Simulation of a jet shape in central Pb+Pb collisions at the LHC (left panel). The ratios of the medium-modified jet shape in heavy-ion collisions to the jet shape in the vacuum for jet energies $E_T = 20, 50, 100, 200$ GeV for $R = 0.4$ (left panel).

$r/R < 0.25$ region of the intra-jet energy flow in p+p collisions in our calculation has uncertainties associated with the normalization of the jet shape. In the moderate and large $r/R > 0.25$ region our theoretical model gives excellent descriptions of the Fermilab Run II (CDF II) data. The QGP effects are manifested as a suppression near the core and enhancement near the periphery of the jet. In the tail of the energy flow distribution for a cone radius $R = 0.4$ this ratio can reach values ~ 1.75 .

§5. Conclusions

In summary, we discussed the discriminating power of jet observables with respect to models of parton propagation and energy loss in the QGP. More stringent constraints on theory, such as the ones that upcoming data on jet production and modification in heavy-ion reactions will provide, are necessary for precision jet tomography and accurate determination of the properties of strongly-interacting nuclear matter. To this end, we presented perturbative QCD calculations of inclusive jet cross sections/shapes and Z^0/γ^* -tagged jets to $\mathcal{O}(\alpha_s^3)$, $\mathcal{O}(\alpha_s^2\alpha_s^{\text{med.}})$ and $\mathcal{O}(G_F\alpha_s^2)$, $\mathcal{O}(G_F\alpha_s\alpha_s^{\text{med.}})$, respectively. To demonstrate the sensitivity of these observables to the characteristics of the vacuum and medium-induced parton showers, we examined their pronounced dependence on the cone radius R at next-to-leading order. Experimental jet physics results in heavy-ion collisions are still very preliminary but agree qualitatively with the theoretical expectations. Future studies in this direction will focus on the inclusion of non-perturbative hadronization effects and extending the NLO calculations of jets at RHIC and at the LHC. In their entirety, these theoretical advances will provide first-principles insights into the many-body QCD parton dynamics at ultra-relativistic energies.

Acknowledgements

I would like to thank KITP for their hospitality and support in the preparation of this brief overview article and my collaborators R. B. Neufeld and B. W. Zhang for helpful discussion. This research is also supported by the US Department of Energy, Office of Science, under Contract No. DE-AC52-06NA25396 and by the LDRD program at LANL.

References

- 1) M. Cacciari, J. Rojo, G. P. Salam and G. Soyez, arXiv:1010.1759 [hep-ph]. G. P. Salam and G. Soyez, JHEP **0705**, 086 (2007) [arXiv:0704.0292 [hep-ph]].
- 2) G. Sterman, S. Weinberg, Phys. Rev. Lett. **39**, 1436 (1977); R. P. Feynman, R. D. Field, G. C. Fox, Phys. Rev. D **18**, 3320 (1978).
- 3) S. Salur, Nucl. Phys. A **830**, 139C (2009); M. Ploskon, Nucl. Phys. A **830**, 255C (2009). Y. S. Lai [PHENIX collaboration], arXiv:0911.3399 [nucl-ex].
- 4) M. Voutilainen, "Studies of QCD jet production with the CMS detector in pp collisions at $\sqrt{s} = 7$ TeV", ICHEP 2010, Paris, France
- 5) N. Grau, Nucl. Phys. A **830**, 797C (2009); D. d'Enterria *et al.*, J. Phys. G **34** (2007) 2307.
- 6) I. Vitev, S. Wicks and B. W. Zhang, JHEP **0811**, 093 (2008); I. Vitev, B. W. Zhang and S. Wicks, Eur. Phys. J. C **62**, 139 (2009).
- 7) R. Baier, Y. L. Dokshitzer, A. H. Mueller, S. Peigne and D. Schiff, Nucl. Phys. B **484**, 265 (1997); B. G. Zakharov, JETP Lett. **65**, 615 (1997); M. Gyulassy, P. Levai and I. Vitev, Phys. Rev. Lett. **85**, 5535 (2000); X. f. Guo and X. N. Wang, Phys. Rev. Lett. **85**, 3591 (2000);
- 8) S. D. Ellis, Z. Kunszt, D. E. Soper, Phys. Rev. Lett. **64**, 2121 (1990); Z. Kunszt and D. E. Soper, Phys. Rev. D **46**, 192 (1992).
- 9) J. M. Campbell, R. K. Ellis, F. Maltoni and S. Willenbrock, Phys. Rev. D **73**, 054007 (2006) [Erratum-ibid. D **77**, 019903 (2008)] J. M. Campbell, R. K. Ellis, F. Maltoni and S. Willenbrock, Phys. Rev. D **69**, 074021 (2004).
- 10) M. H. Seymour, Nucl. Phys. B **513**, 269 (1998). S. D. Ellis *et al.* Prog. Part. Nucl. Phys. **60**, 484 (2008).
- 11) B. I. Abelev *et al.* [STAR Collaboration], Phys. Rev. Lett. **97**, 252001 (2006).
- 12) I. Vitev and B. W. Zhang, Phys. Rev. Lett. **104**, 132001 (2010).
- 13) I. Vitev, Phys. Lett. B **630**, 78 (2005). I. Vitev, Phys. Rev. C **75**, 064906 (2007).
- 14) I. Vitev, Phys. Lett. B **562**, 36 (2003) [arXiv:nucl-th/0302002]. I. Vitev, B. W. Zhang, Phys. Lett. B **669**, 337 (2008); R. Sharma, I. Vitev, B. Zhang, Phys. Rev. C **80**, 054902 (2009); R. B. Neufeld, I. Vitev and B. W. Zhang, arXiv:1010.3708 [hep-ph].
- 15) D. K. Srivastava, C. Gale and T. C. Awes, Phys. Rev. C **67**, 054904 (2003); G. J. Kunde, H. van Hecke, K. Hessler and C. Mironov, Eur. Phys. J. C **61**, 785 (2009). I. P. Lokhtin, A. V. Sherstnev and A. M. Snigirev, Phys. Lett. B **599**, 260 (2004).
- 16) R. B. Neufeld, I. Vitev and B. W. Zhang, arXiv:1006.2389 [hep-ph].
- 17) D. E. Acosta *et al.* [CDF Collaboration], Phys. Rev. D **71**, 112002 (2005).